CHAPTER 4

Effect of Cl Doping on Structural and Electrical Properties of Exfoliated WS_2 Nanosheets

Contents:

4.1. Introduction:

Ultrathin semiconducting layered TMD materials, like WS_2 nanosheets, possess excellent structural and morphological properties, tunable bandgap, and outstanding physical and electrical properties. These characteristics make them ideal candidates for applications in microelectronics and nanoelectronics [1–3]. Due to its remarkable properties and n-type semiconducting nature, the WS_2 serves as an effective channel material in semiconductor devices and offers the potential for scalability in both size and thickness [4–6]. Despite its unique features, WS_2-based semiconductor devices face many obstacles that need to be addressed for successful application in electronic devices. One of the major issues is that WS_2 has high sheet resistance. In addition, the interface between WS_2 and metal contacts plays an important role in semiconductor engineering. Numerous studies have reported that M-S interfaces often exhibit high contact resistance, which can hinder carrier transport across the junction and contribute to an increase in the SBH as schematically depicted in Fig. 4.1(a).[7,8]. The R_C at the junction of metal and few-layered WS_2 consists of two resistances in series: Schottky Barrier Resistance (R_{SB}) and Interlayer Resistance (R_{IL}) [9, 10]. The R_{SB} and R_{IL} exhibit the tunneling resistance from metal to semiconductor across the schottky barrier and interlayer injection resistance between parallel 2D planes, as illustrated in Fig. 4.1(b). R_{SB} is determined by the Schottky barrier height at the Metal-WS_2 interface, which depends on the mismatches of metal (Φ_M) and Semiconductor Work Function (Φ_S). Additionally, the R_{IL} arises from the resistance between two adjacent WS_2 layers. However, the R_{IL} in the WS_2 channel remains constant and is unaffected by the type of metal used for contact. The primary focus is on reducing R_{SB} by lowering the SBH at the M-S interface, as reported in various studies. The higher SBH at the M-S interface can be attributed to several factors, including the binding energy between the metal and semiconductor atoms and the mismatch between their respective work functions [11,12]. Additionally, the stoichiometry of WS_2 nanosheets is affected during the synthesis, exhibiting voids where some atoms are absent from the crystal lattice [13–15]. Also, the vacancies can disrupt the electron transport in WS_2, leading to a reduction in electrical conductivity and disrupting the transistor switching behaviour [16,17]. The primary contributors to the high R_C and SBH are the strong Fermi-level pinning (FLP) effects at the M-S interface, which pin the Fermi Level (E_F) near the Charge Neutrality Level (E_{CNL}), as illustrated in

Fig. 4.2(a) [18]. For certain TMDs, such as WS_2, the E_{CNL} is situated near the mid-gap, resulting in a higher SBH. This increases the difficulty of achieving low R_C. This phenomenon hinders the formation of ohmic contact by maintaining a significant energy barrier, which reduces carrier injection efficiency across the interface [19]. However, those limitations can be controlled by modulating the Barrier Height (Φ_B) at the M-S interface through various techniques such as interface engineering by selecting metals with low work functions for the contacts [20], doping [21] and introducing a passivation layer [22]. These approaches optimize the SBH and R_C, improving carrier injection and enhancing overall device performance.

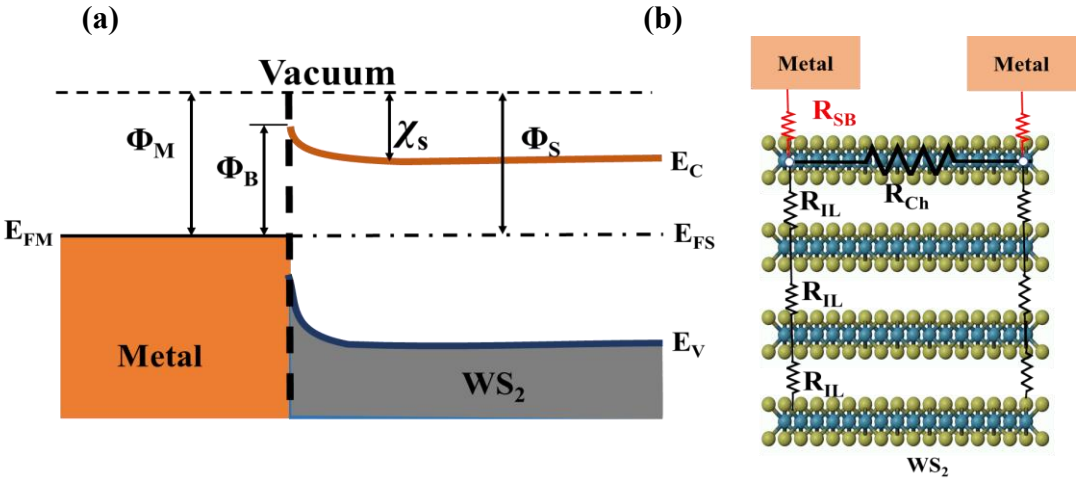

Fig. 4.1: (a) Schematic representation of the energy band diagram at the metal-semiconductor interface, defining the Φ_B and (b) Resistor network model of the multilayer 2D material with metal contact, illustrating the presence of resistances R_{SB} and R_{IL}

4.1.1. Impact of Metal Work-Function on Contact Properties in TMD Materials:

Recent research has highlighted the role of interface engineering in optimizing the performance of 2D material-based devices. Previous studies have shown that metals such as Au (5.2 eV), Pt (5.6 eV), Pd (5.1 eV), and Ni (5.1 eV) present high Schottky barrier heights when they make contact with 2D-TMD materials. This is attributed to the significantly higher Metal Work Functions (Φ_M) of these metals compared to those of TMD materials like WS_2, MoS_2, etc. [23–27]. The elevated SBH negatively impacts the device's current transport characteristics, leading to an increase in contact resistance R_C.

However, the use of lower work-function metals like Sc (3.5 eV), Ti (4.3 eV), In (4.12 eV), etc. can help to reduce the R_C and SBH at the M-S interface as reported by Das et al., Tang et al. and Phan et al. [20, 28, 29].

WS_2 in contact with high work-function metals typically exhibits a vdW gap at the interface, resulting from weak physical interactions between the metal and semiconductor [30]. In contrast, an ideal contact can be achieved using low work-function metals, where stronger interactions lead to covalent bonding between the metal and semiconductor atoms. This covalent bonding minimizes the vdW gap and improves charge injection, reducing both the SBH and R_C, as schematically illustrated in Fig. 4.2 (b). However, in practical scenarios, FLP is influenced by factors such as interfacial dipoles, Metal-Induced Gap States (MIGS) and interfacial defects. The work function of metal influences the electronic band structure at the M-S interface, owing to FLP effect. When metals with work functions (like Sc, Ti) come in contact with WS_2 or MoS_2, the E_F of the semiconductor aligns closer to the conduction band of the TMD [14,20]. This alignment results in n-type contact characteristics, reducing the SBH for electron injection and allowing electrons to move freely across the vertical interface. Consequently, these metals can promote effective electron injection into the conduction band, and under ideal conditions, they may also create ohmic contacts. Conversely, metals with higher work functions (such as Ni, Pt, Au) position the E_F near the valence band of WS_2 or MoS_2 [14]. This results in an elevated Schottky barrier rendering high resistance to electron injection. Nonetheless, the alignment with the valence band-aids in hole injection, allowing p-type contact characteristics. These metals are especially valuable for uses that demand effective hole transport, like p-type transistors or optoelectronic devices dependent on hole injection. However, reducing the R_C and SBH solely by tuning the work function of metal contacts remains challenging. This phenomenon is attributed to the FLP effect, which arises from the formation of interface states at the Metal-TMD interface [22]. These interface states are typically caused by defects, impurities, or the chemical bonding interactions between the metal and the TMD. These states create an energy barrier that effectively "pins" the Fermi level at a specific position, making it difficult to freely shift the Fermi level to align with the desired band edges (conduction or valence band). This pinning typically takes place near the effective E_{CNL} a critical energy level where the net charge transfer between the metal and the TMD interface is zero [31]. In TMDs, the E_{CNL} is often located close to either the conduction band or the valence band, depending on the

doping type and the material's intrinsic properties. This proximity restricts the Fermi level's tunability because the E_F tends to align with the E_{CNL} regardless of the work function of the metal contact. As a result, the SBH is determined more by the E_{CNL} position than by the metal's intrinsic properties [32]. This behaviour poses a significant challenge in achieving low contact resistance, which is crucial for efficient charge injection in electronic devices. High contact resistance leads to energy losses, reduced current flow, and degraded device performance, making it one of the key bottlenecks in optimizing TMD-based electronic and optoelectronic devices. Understanding and mitigating the effects of FLP and the E_{CNL} is essential for advancing the practical application of TMDs. Additionally, surface defects or vacancies can introduce localized energy states that trap charges, preventing the E_F from aligning with the metal's work function [33]. Charge redistribution at the interface can generate dipoles, altering the effective barrier height. Furthermore, a smaller contact area can limit charge transport, thereby increasing the SBH and R_C. Without surface modification, another effective strategy for modulating the SBH involves introducing an interfacial layer at the interface of the M-S.

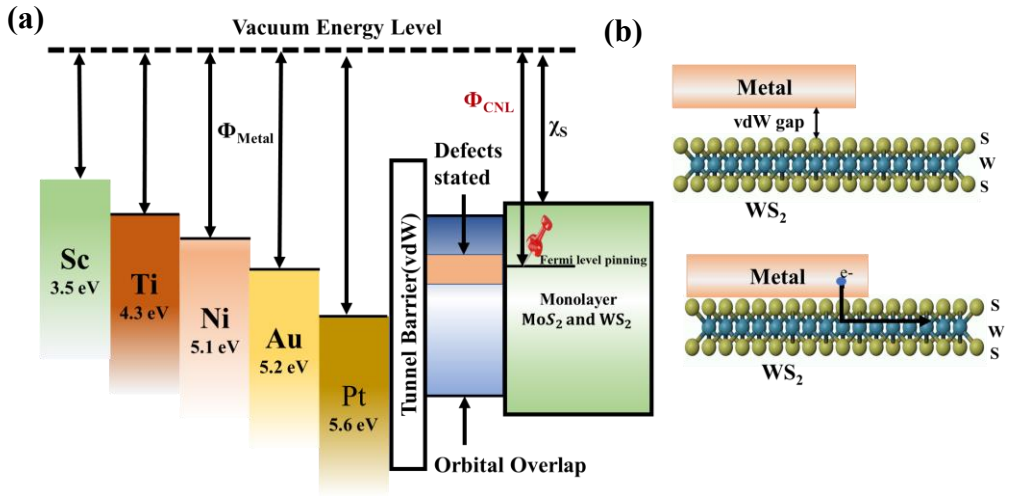

Fig. 4.2: (a) The Band diagram at the contact illustrates interface states, including the tunneling barrier, vdW gap, orbital overlap of the TMD under the metal, and defect states. These factors can modify the SBH and lead to FLP and (b) Metal-WS_2 contact with a high work-function metal typically exhibits a van der Waals gap, whereas an ideal contact can be achieved using a low work-function metal

4.1.2. Strategy to Improve the M-S Interface by Inducing the Interfacial layer:

The use of an interfacial layer has been extensively studied in bulk semiconductors such as Si [34], germanium (Ge) [35], and III-V materials [36, 37] for the reduction of SBH in M-S junction. The interfacial layer reduces the direct interaction between the metal and the semiconductor, thereby mitigating the FLP effect. From previously reported results, it has been established that incorporating a thin dielectric layer, such as Al_2O_3 [22], Hexagonal Boron Nitride (h-BN) [38], etc., between the metal and TMD junction effectively reduces the SBH. A recent study by Zheng et al. and Phan et al. reported the impact of Al_2O_3 and h-BN as interfacial layers in WS_2 FETs with Cr metal contacts, showing a reduction in SBH from 0.58 eV to 0.22 eV for Al_2O_3 and from 0.04 eV to 0.02 eV for h-BN [22, 29]. The findings revealed that this Metal-Insulator-Semiconductor (MIS) contact configuration significantly broadens the range of controllable SBH, thereby facilitating Fermi level depinning, as depicted in Fig. 4.3 [22, 31]. The ultrathin dielectric layer placed between the metal and WS_2 acts as a depinning layer, enabling Fermi level adjustment and lowering the SBH at the junction. This effect is attributed to the dielectric layers ability to mitigate gap states caused by defects at the interface. Fine-tuning the thickness of the interfacial layer is crucial, as it significantly influences the SBH. Optimizing this thickness can enhance key device performance parameters, such as on-current, I_{ON}/I_{OFF} ratio, and field-effect mobility. The performance of the device is highly influenced by the thickness of the interfacial layer; however, its inclusion necessitates precise deposition techniques, complicating the fabrication process and potentially increasing the manufacturing costs. Additionally, introducing an interfacial layer may inadvertently modify the band alignment, leading to undesirable electronic properties.

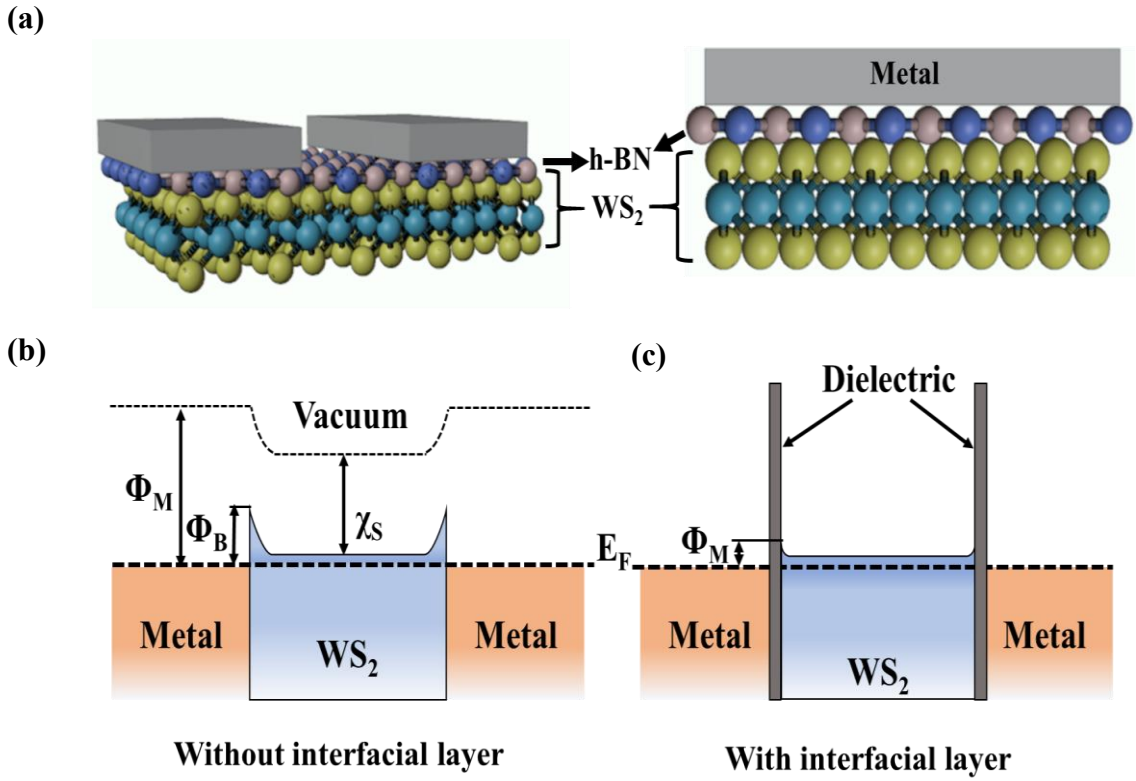

Fig. 4.3: (a) Schematic representation of a MIS structure, where h-BN serves as the interfacial layer between the metal and the semiconductor, along with the energy band diagram of WS_2: (b) Energy band diagram of WS_2 without the interfacial layer, and (c) Energy band diagram of WS_2 with the interfacial layer

4.1.3. Surface Modification by Dopant Atom to Improve the M-S Junction:

Over the past few decades, several strategies have been developed to improve the M-S interface through surface modification. These methods include charge transfer, carrier injection, ion implantation, plasma treatment, substitutional doping, and surface doping [39–42]. Each of these techniques aims to introduce donor or acceptor states on the semiconductor surface, thereby enhancing the interface, electrical properties and optimizing device performance.

Nevertheless, to meet the diverse demands of future electronic devices, the electrical properties of TMDs ideally require to be controlled through doping, which is crucial for achieving high conductivity, improved carrier mobility, and low barrier heights. Various dopant materials have been employed to extend the doping capabilities

of TMDs [21,40,41]. Doping involves deliberately introducing foreign atoms or impurities into the crystal lattice of the WS_2 is one of the key techniques for effectively modifying its physical properties and enhancing its functionalities such as atomic defects, vacancies, or impurities, which significantly modify the material's electronic behaviour. [45]. Furthermore, doping enhances the electrical performance of WS_2 devices by increasing the carrier concentration and improving channel conductivity, making it well-suited for high-efficiency transistor applications [46]. The controlled structural modifications achieved through doping facilitate bandgap tuning, defect engineering, reduced contact resistance, and optimized barrier height, thereby enhancing carrier concentration and mobility [41,43]. These improvements significantly broaden the applicability of WS_2 in advanced transistor technologies.

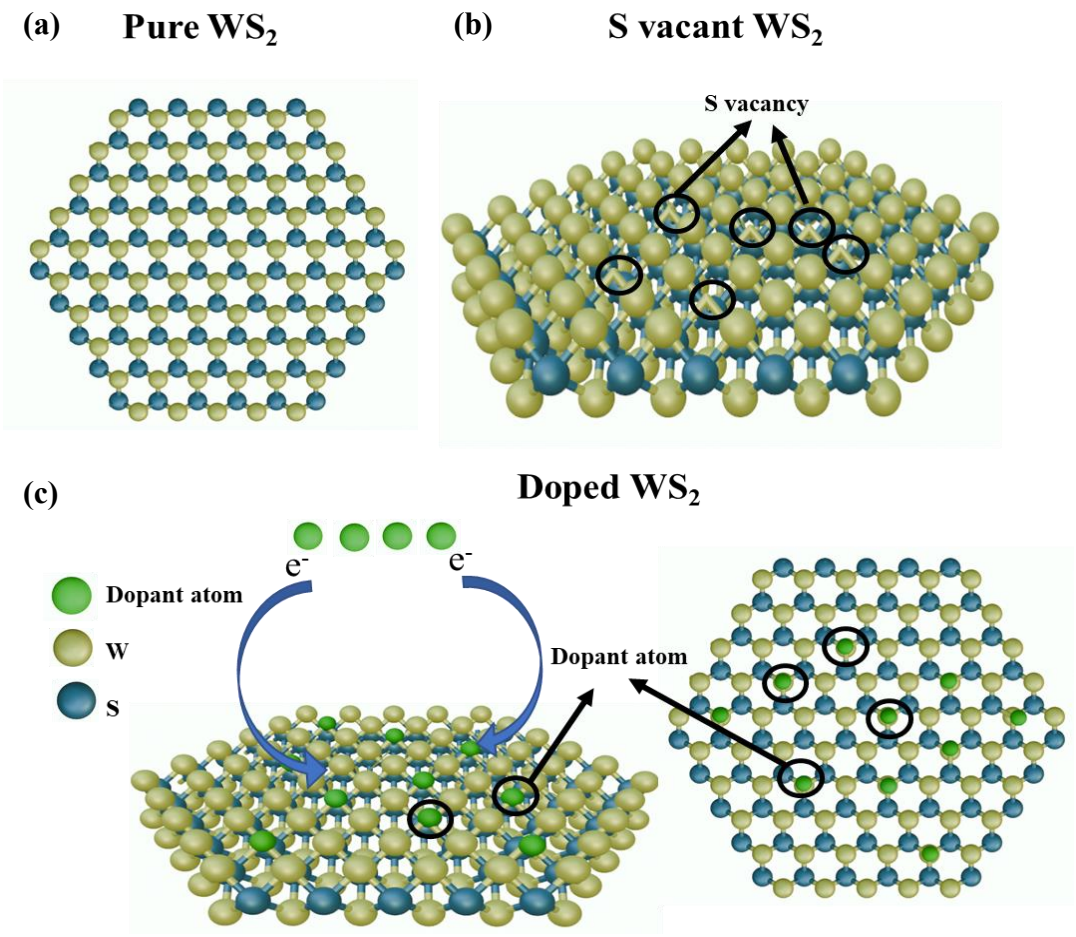

Fig: 4.4: Schematic illustration of the atomic lattice of (a) pure WS_2 (b) S vacant WS_2 and (c) the doping process of a WS_2 monolayer with an n-type dopant atom

Table 4.1: Variation of SBH, R_C and Mobility in TMD-based transistor devices with work-function dependent metal contacts or n-type doping

TMD	Dopant atom	Metal/interfacial layer	Doping Time	R_C	SBH (eV)	Mobility ($cm^2/V.s$)	Ref. No.
MoS_2	-	SC	-	-	0.03	184	[20]
	-	Ti	-	-	0.05	125	
	-	Ni	-	-	0.15	36	
	-	Pt	-	-	0.23	21	
WS_2	LiF	-	2 min	31.2 - 0.9 kΩ.μm	-	13.2 - 34.7	[21]
WS_2	-	In	-	~10^3 kΩ.μm	0.01	-	[29]
	-	Cr	-	~10^3 kΩ.μm	0.04	-	
	-	Single layer h-BN	-	0.18 MΩ.μm	0.20	115	
	-	Double layer h-BN	-	1.19 MΩ.μm	0.24	-40	
WS_2	Hydrazine	-	0-12 min	-	-	25 - 75	[47]
WS_2	Cu	-	-	7.4×10^6 Ω.μm	0.89	4.9 - 21.9	[48]
	Cu	Cu	-	1×10^6 Ω.μm	0.50	26.3	
WS_2	Cl	-	>12 hr	10^2 - 0.7 kΩ.μm	-	60	[49]
WS_2	Li	-	-	-	-	0.076 - 4.246	[46]
WS_2	(RhCp∗Cp)2	-	0-10 min	1140 - 7 kΩ.μm	0.112 - 0.057	2.4 - 4.2	[50]

However, the surface doping process alters the TMD materials' structural and electronic properties by tuning atomic defects, the energy bandgap, and exciton physics [51]. The n-type dopant materials such as Potassium Iodide (KI) [4], Lithium Fluoride (LiF) [21], Hydrazine [47],Copper (Cu) [48], Iron (Fe) [52], and others have been used to improve stoichiometry by reducing defects and impurities, thereby enhancing the n-type characteristics in 2D TMD materials. These dopants improve stoichiometry by reducing defects and impurities, which in turn minimizes atomic vacancy states within the atomic lattice of the 2D material, as schematically depicted in Fig. 4.4. This defect passivation improves carrier transport properties by introducing additional charge carriers (donor atoms with extra electrons), thereby enhancing the n-type characteristics of WS_2. Consequently, these modifications result in improved conductivity, higher carrier

mobility, and better performance in electronic and optoelectronic applications. In traditional semiconductors, doping is achieved through the injection or diffusion of charge carriers. However, accurately controlling the doping density becomes difficult when using ion implantation techniques for thin semiconductor materials, especially when their thickness is only a few nanometers [42,46,48]. Molecular doping offers several advantages, including the requirement for a simpler experimental setup compared to high-temperature or high-energy particle-based doping methods. Additionally, it enables the formation of isotropic doping profiles, ensuring uniform distribution of dopants throughout the material [54]. Table 4.1 provides a comprehensive summary of the impact of n-type doping inclusion of interfacial layer Metal-WS_2/MoS_2 on the electrical performance including parameters such as contact resistance, Schottky barrier height, and mobility.

In this study, demonstrate Cl doping of LPE-processed WS_2 nanosheets by adsorption technique, effectively reducing the R_C and SBH at the M-WS_2 junction. The n-type doping process includes the introduction of donor atoms that can remove atomic vacancies, defects, or impurities in the atomic lattice of the semiconductor. A time-dependent doping process was employed to optimize the electrical and chemical properties of WS_2 nanosheets and evaluate material quality. The quality of the doped WS_2 was assessed using various spectroscopic and imaging techniques, including Raman spectroscopy, PL, XRD, energy-dispersive X-ray (EDX) spectroscopy, and FESEM. This analysis helped to determine whether doping negatively impacted the material's structural and chemical integrity. The electronic properties of the WS_2 nanosheets, such as contact resistance, Schottky barrier height, I_{ON}/I_{OFF} ratio, and conductivity of the WS_2 device, were optimized through I-V measurements. Doping significantly improved the electrical transport characteristics, attributed to a reduction in SBH at the Metal-WS_2 interface. This reduction lowered the conduction band edge, enabling electron transport across the junction at relatively low bias and enhancing electrical conductivity. Additionally, temperature-dependent studies were conducted in the range of room temperature to 100 ^oC. The I-V measurements revealed a notable increase in on-current with rising temperature for both doped and undoped WS_2 devices, driven by thermally generated charge carriers crossing the junction. To further investigate the energy bandgap and material properties of undoped and doped WS_2, DFT simulations were performed using

Quantum Espresso. These simulations provided deeper insights into the electronic structure and doping effects on WS_2 nanosheets, confirming the experimental findings.

4.2. Experimental Procedure for Doping:

The LPE processed few layers of WS_2 nanosheets were doped with Cl using molecular doping technique. The as prepared WS_2 nanosheets is first deposited onto the SiO_2-coated Si substrate and annealed at 60 ^oC for approximately 6 hr in a vacuum oven to remove moisture and impurities from the nanosheet surface. Then the exfoliated few-layer WS_2 nanosheets were soaked into the 1,2-Dichloroethane (DCE) solution for varied durations (6 hr to 24 hr) to dope WS_2 nanosheets with Cl atoms. After the soaking, the nanosheets were rinsed with Acetone and IPA followed by drying at ~60 ^oC in an oven to remove the unwanted residues from the nanosheet surface. The doping process is pictorially illustrated in Fig 4.5. The electrical measurements were done to investigate the effect of doping on the conduction property of the doped semiconductor. In order to perform the I-V measurement silver paste was used as the metal contact on both undoped and doped WS_2 nanosheets. A shadow mask was utilized to define the channel and contact areas, after which the silver paste was applied to the nanosheet surface and dried in a vacuum environment. The resulting device has channel dimensions of approximately 100 μm in Length (L) and 500 μm in Width (W). A detailed summary of the doping steps is provided in Table 4.2.

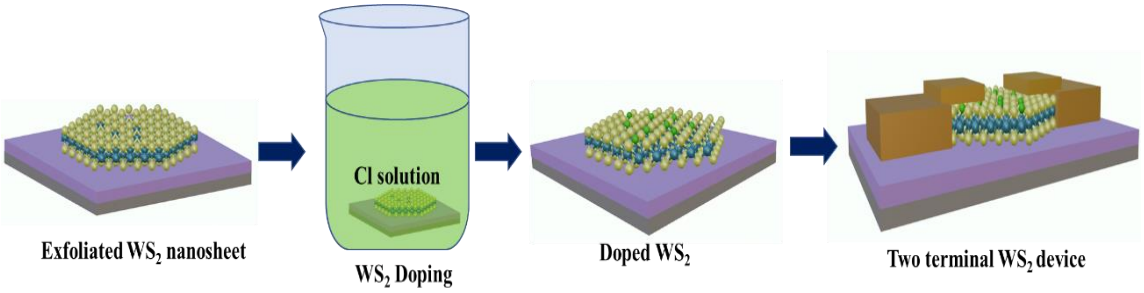

Fig 4.5: Schematic representation of the molecular doping technique

Table 4.2: Process summary of molecular doping of WS_2 using 1,2-dichloroethane

Process Stage	Process Stage	Materials / Tools Used
Substrate Preparation	SiO_2-coated Si substrate	Substrate cleaned and prepared for nanosheet deposition
WS_2 Deposition	WS_2 nanosheet	spin-coated onto the substrate
Pre-Annealing	Vacuum oven	60 °C for ~6 hours to remove moisture and surface impurities
Doping Treatment	DCE	Samples soaked for varying durations: 6 hr, 12 hr, 18 hr, and 24 hr
Post-Annealing	Vacuum oven	60 °C
Contact Formation	Silver paste, shadow mask	Channel defined using shadow mask; Ag paste applied and vacuum dried
Device Structure	Channel dimensions	L = 100 μm and W = 500 μm

4.3. Energy Band Calculation of WS_2:

Density Functional Theory (DFT) study using BURAI software Graphical User Interface (GUI) programme of QUANTUM-ESPRESSO (QE)) is employed to investigate the effect of Cl doping on conduction properties of WS_2 nanosheets. Fig. 4.6 illustrates the substitutional doping of Cl atoms in a double-layered 3 x 3 x 1 superlattice of WS_2 modelled in QE. In this study, the energy bandgap was calculated to confirm that the properties of WS_2 remain unaffected by Cl doping. The dopant material (Cl atoms), induces n-type doping, and the interaction between chlorine and the WS_2 nanosheets is examined by analyzing the energy band structure. Fig.4.6 presents the bandgap of pure WS_2, as well as WS_2 superlattices with O and Cl occupying S vacancy sites, along with the distribution of energy states, as determined by the Density of States (DOS). For the pristine WS_2, the calculated bandgap is approximately 1.62 eV, which suggests that the material exhibits an indirect bandgap characteristic. After introducing a sulfur vacancy, which is then filled by an O atom, the bandgap decreases slightly to around 1.5 eV. On the other hand, chlorine-doped WS_2 shows a more significant alteration, with the bandgap widening to approximately 1.8 eV.

In O-occupied WS_2, a reduction in the bandgap is observed, with the CBM located at the K-point and the VBM at the Γ-point, as illustrated in Fig. 4.6(b). Additionally, the VBM shifts closer to the Fermi level than pristine WS_2. This shift signifies a transition towards a more indirect bandgap nature, influenced by the presence of a single O atom, which can impact the energy bandgap properties of WS_2. In the case of chlorine doping, chlorine atoms are adsorbed onto sulfur vacancy sites within the WS_2 supercell [55]. Fig. 4.6(c) depicts the energy band structure of Cl-doped WS_2, showing a noticeable shift of

the conduction band toward the E_F and the emergence of mid-gap states near E_F [44]. The energy band shift is accompanied by the splitting of the conduction band into two distinct sub-bands, which emerge between high-symmetry points in the Brillouin zone, as shown in the enlarged depiction of the energy bandgap in Fig. 4.6(c). This band splitting is a result of defect states introduced by the hybridization of chlorine's 3p orbitals with tungsten's 5d orbitals [44]. When chlorine atoms occupy sulfur vacancy sites, their 3p orbitals overlap with tungsten's 5d orbitals, modifying the electronic structure and creating localized states within the bandgap. This interaction alters the conduction band's energy levels, leading to the observed splitting and significant changes in the electronic properties of the material.

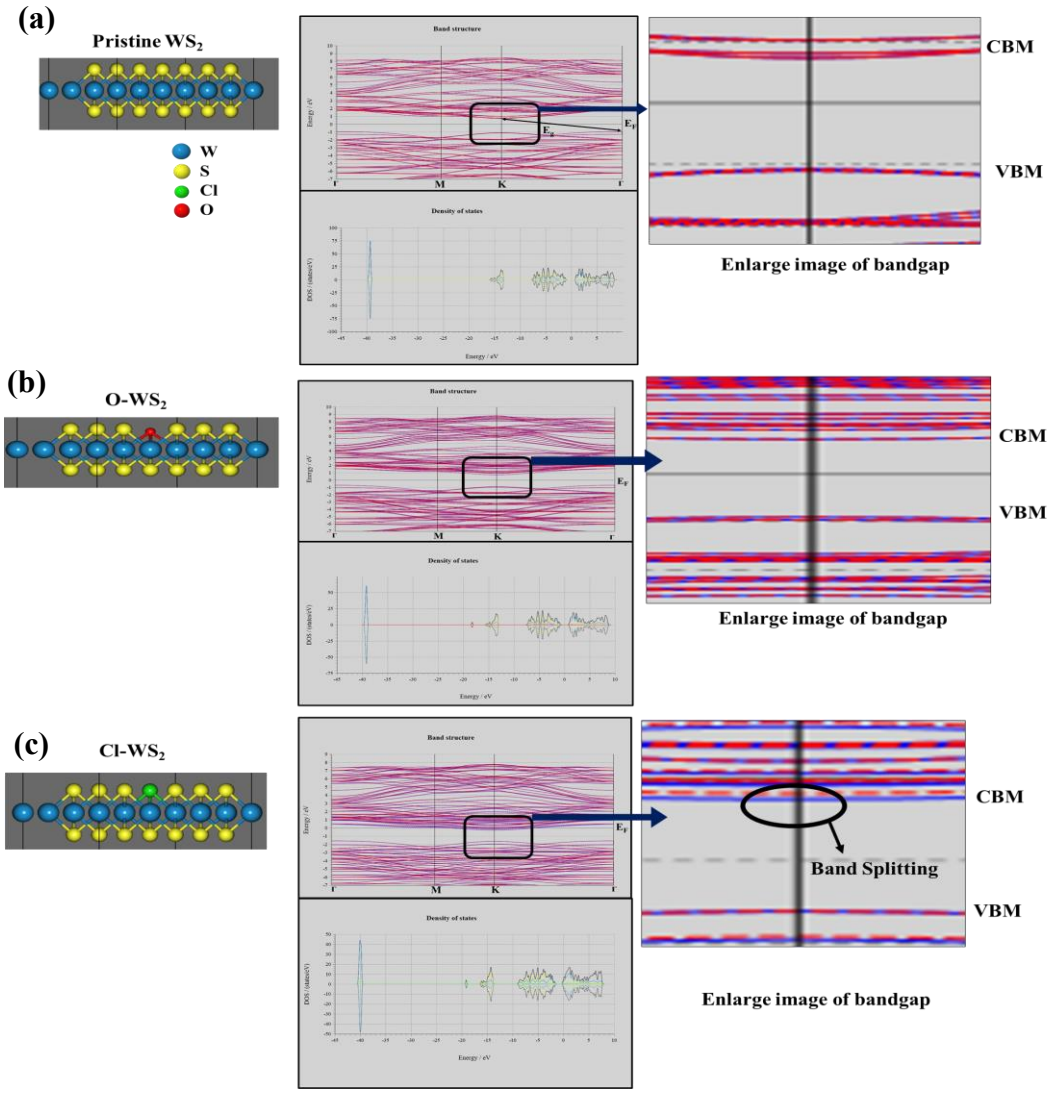

Fig. 4.6: DFT calculated energy band diagram and DOS for (a) pure WS_2 (b) WS_2 with an O atom and (c) Cl atom occupying a sulfur vacancy site in the WS_2 supercell.

The doping introduces an additional unpaired electron due to chlorine's n-type doping nature, further influencing the energy levels of the tungsten d-orbitals. Since tungsten is located in the 6th period of the periodic table, the additional negative charge from chlorine atoms induces the splitting of the W 5d orbitals, leading to the formation of mid-gap states. The doping effect can cause a shift in the position of the bands compared to undoped WS_2 and O-WS_2, reflecting changes in the atomic structure and the hybridization between chlorine and tungsten orbitals. The shift in the conduction band towards the Fermi level demonstrates the impact of n-type doping from chlorine on the sulfur vacancy site, enhancing the material's conductivity [56].

4.4. Spectroscopy Analysis of Undoped and Doped WS_2 Nanosheet:

The structural and morphological properties of WS_2 nanosheets after doping were studied through spectroscopy analysis using Raman spectroscopy, PL, XRD, FESEM, and EDX. The time-dependent doping effect due to soaking of the exfoliated WS_2 nanosheet in Cl for 6 hr to 24 hr is studied using Raman spectroscopy data as depicted in Fig. 4.7(a & b). The characteristics of the 2D material were investigated by studying the first-order acoustic modes of two frequency peaks: the A_{1g} mode (out-of-plane vibrations) and the E^1_{2g} mode (in-plane vibrations) [4]. Both the A_{1g} and E^1_{2g} peaks intensity of the doped WS_2 nanosheets was found to increase with the increasing of Cl absorption time which probably is due to the stoichiometry of WS_2 and reduction of defects or sulfur vacancies in the lattice [57]. The position of the frequency peaks A_{1g} and E^1_{2g}, and the disparity between the peaks ~65 cm^{-1} remains unchanged even after 24 hr of doping. The intensity ratio of the two peaks increased with increasing doping time, the results align with the reported results [43, 46, 58].

Fig. 4.7 (c & d) illustrates the PL spectra of n-type Cl-doped WS_2 nanosheets at room temperature. In the PL spectrum, a prominent and intense emission peak appears at ~649 nm for exfoliated WS_2 nanosheets [43]. A red shift in the PL emission spectra, along with a gradual decrease in intensity, was observed as the duration of Cl adsorption onto the WS_2 surface increased from 6 hr to 24 hr as shown in Table 4.3. This shift indicates that the incorporation of Cl atoms significantly affects the light-emission characteristics of WS_2 nanosheets. Moreover, with an increase in n-type Cl dopant concentration, electrons tend to combine with excitons (bound electron-hole pairs), resulting in their conversion into trions (charged excitons) [59]. The concentration of negatively charged trions

increased with higher doping levels, attributed to enhanced electron injection, suggesting that the Cl atoms act effectively as n-type dopants in WS_2 nanosheets. To better understand the Exciton (A^o) and Trion (A^-) Emissions, the PL spectra were deconvoluted using a Lorentzian distribution, as shown in Fig. 4.7(d) [16,42,57]. After 24 hr of Cl doping, the A^- intensity increased while A^o decreased, indicating that prolonged Cl doping alters the behaviour of WS_2 thin films by reducing vacancy or defect states in the atomic lattice and enhancing their n-type characteristics [33].

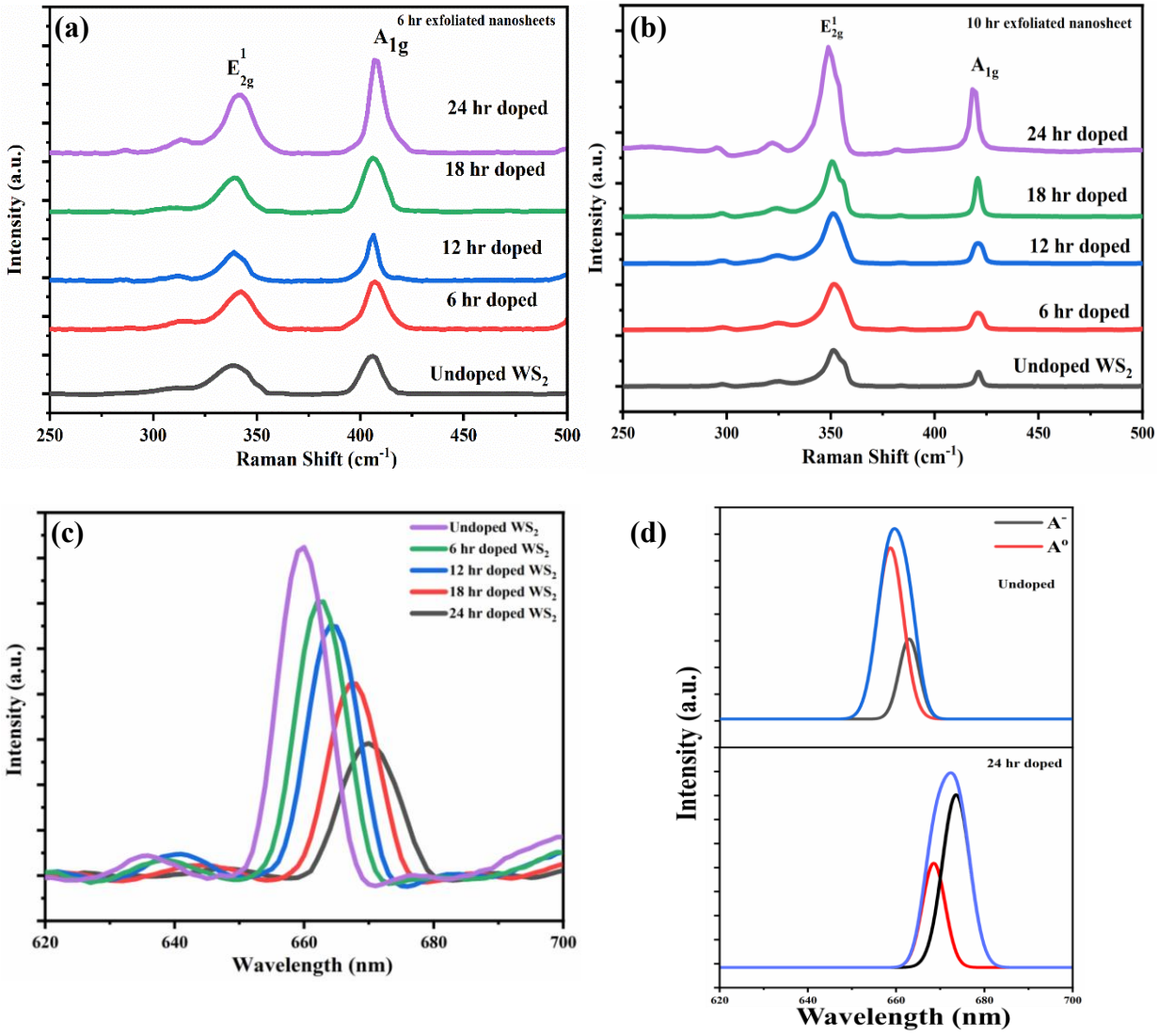

Fig. 4.7: Illustrates spectroscopic analysis for the Undoped and Cl doped WS_2 thin-film: (a & b) Raman spectroscopy for 6 hr and 10 hr exfoliated nanosheets, (c & d) PL Spectroscopy analysis

Table 4.3: Shift of PL peak with varying doping time

Doping Time	PL Intensity Shift (nm)
Undoped	659.7
6 hr	662.5
12 hr	664.6
18 hr	667.9
24 hr	669.6

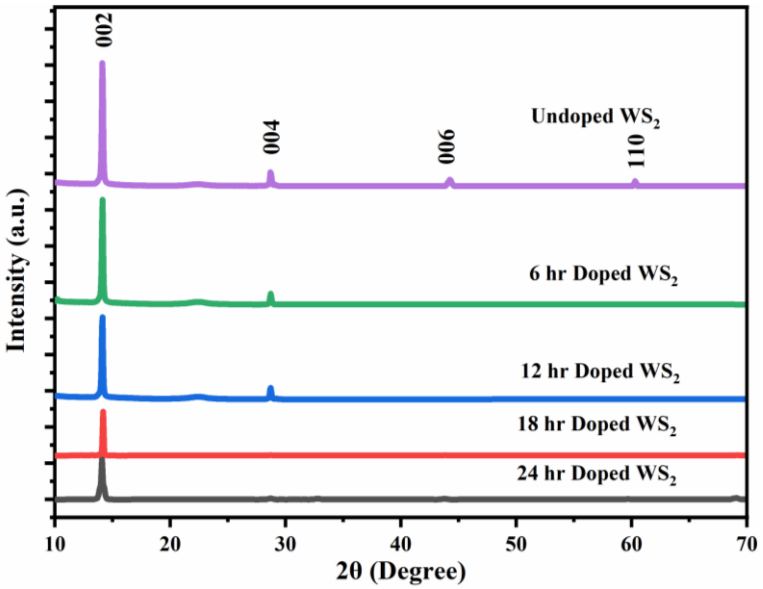

Fig. 4.8: XRD analysis of the undoped and doped WS_2 nanosheets with varying the doping time

In addition, the XRD analysis was conducted to assess the crystalline property of WS_2 nanosheets. The multiple diffraction peaks located at 14.6°, 28.6°, 44.20°, and 60.14°, corresponding to the (002), (004), (006), and (110) planes of WS_2, based on the JCPDS#08-0237 reference, as shown in Fig. 4.8 [61, 62]. The prominent peak at 14.6° for undoped WS_2 and 14.3° for WS_2 doped for 24 hr. Significantly, the 002 diffraction peak appears consistently across all samples, confirming that the crystal planes maintain a dominant c-axis orientation regardless of doping duration. This observation implies that the doping process preserves the structural integrity of the WS_2 crystal lattice without causing disruption. After doping for 24 hr, the peak of the (002) crystal plane shifted left by 0.3 degrees, with the disappearance of the other diffraction peaks. The reduction in peak intensity suggests that surface vacancies or impurities in WS_2 can be effectively replaced through Cl doping. According to the calculations using Bragg's equation, the

lattice constants for exfoliated and doped WS_2 samples were determined to be 12.2 Å and 12.3 Å, respectively [60,61]. Additionally, the lattice spacing of exfoliated and doped WS_2 nanosheets was found to be 0.6 nm and 0.62 nm, respectively. The obtained data closely aligns with the values reported in our previous HRTEM analysis [65]. The estimated lattice constants of the Cl-doped material remain unchanged and confirm that the structural stability of WS_2 is unaffected by doping. The lattice constant is the distance between repeating units in a crystal lattice, and lattice spacing is the distance between adjacent layers in the crystal structure. However, slight variations observed in the XRD spectra between doped and undoped samples suggest that the crystal structure of WS_2 remains largely unaffected by the doping process.

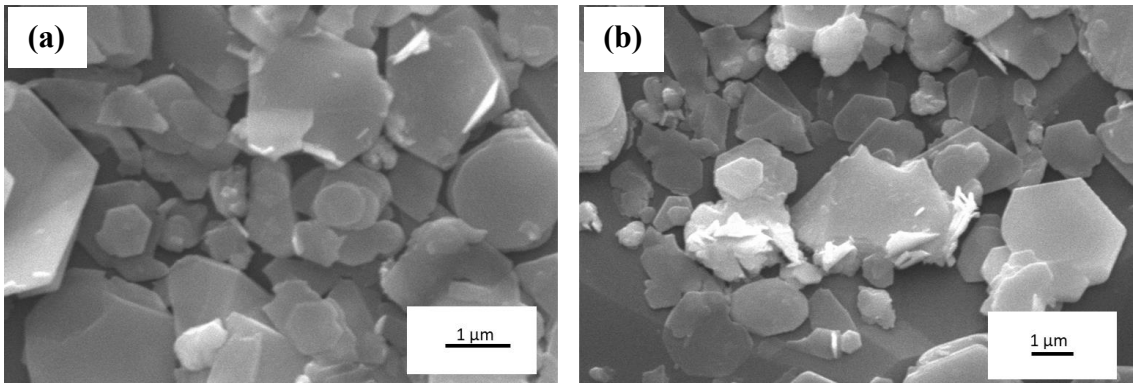

Fig. 4.9: (a) and (b) represent the FESEM images for undoped and 24 hr Cl doped WS_2 nanosheets

The FESEM images of the undoped and Cl-doped WS_2 nanosheets deposited on a Si substrate after drying at 60 ^oC are shown in Fig. 4.9 (a & b). The image reveals an irregular arrangement of hexagonal flakes with a smooth surface without any surface deformation. These flakes are distributed evenly across the entire sample surface [45]. The grain size of the exfoliated WS_2 nanosheets are few microns in size with a hexagonal symmetry. The hexagonal flakes demonstrate a thin, few-layer stacked structure of WS_2, which is suitable for semiconductor device applications.

The EDX spectra were analyzed of undoped and Cl-doped WS_2 nanosheets, are shown in Fig. 4.10(a-e) and elemental color mapping for W, S, O, and Cl is depicted in Fig. 4.10(f-i). The data indicate that a small amount (atomic% of ~0.32) of Cl atoms, observed in the EDX spectra, was adsorbed onto the WS_2 nanosheet surface during the doping. The findings demonstrate that the dopant atoms can be absorbed on the WS_2

nanosheet surface by occupying atomic vacancies or defect states within the atomic lattice [59,60]. Therefore, a material with more atomic vacancies in its lattice and extended exposure to a suitable dopant solution is likely to exhibit a higher degree of vacancy filling by dopant atoms. Table 4.4 summarizes the atomic percentages of O, S, Cl, and W for both undoped and doped WS_2 samples. Notably, Cl doping is accompanied by a relative decrease in oxygen content and a redistribution of sulfur and tungsten levels, particularly evident at longer doping durations. These observations indicate that the dopant atoms effectively fill vacancy sites and contribute to lattice passivation. The increasing Cl content with doping time reflects a greater degree of vacancy occupation, emphasizing the importance of both defect density and exposure time in achieving efficient doping.

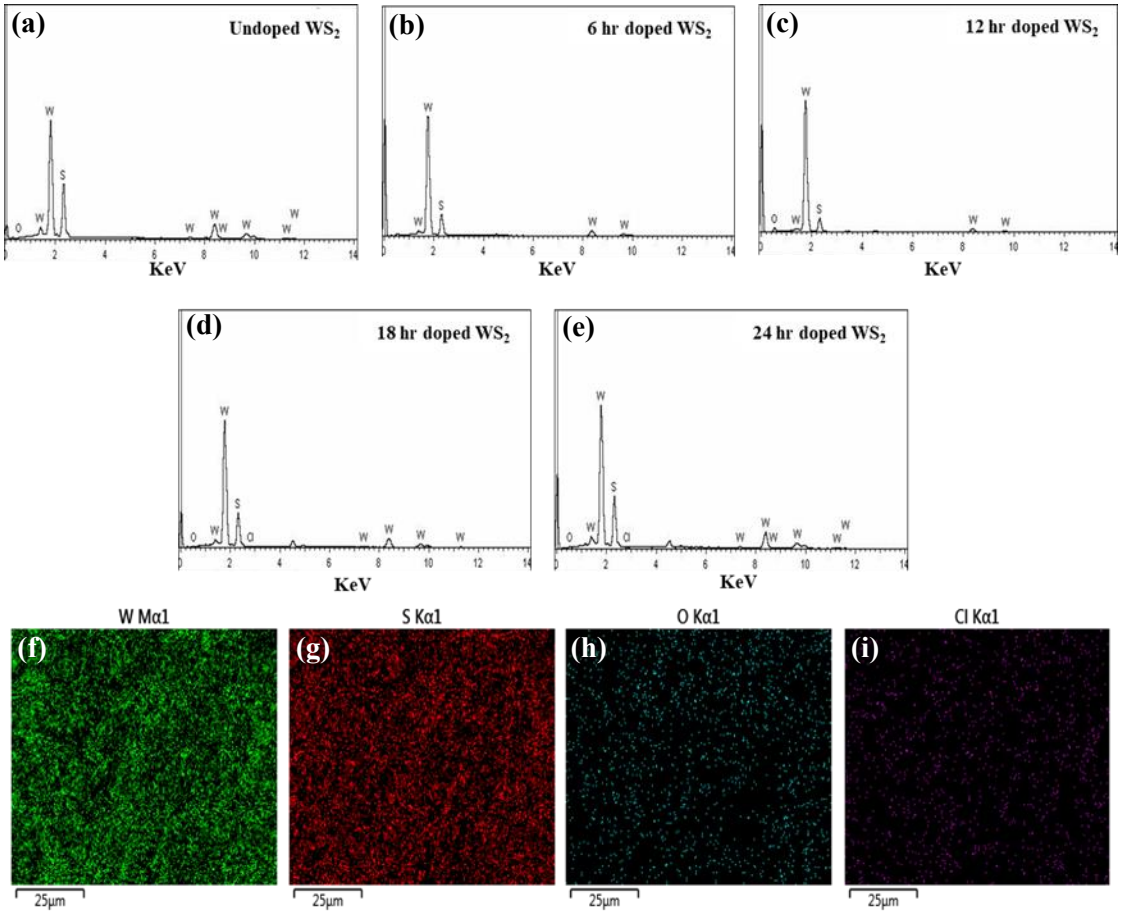

Fig. 4.10: (a-e) Represents the EDX spectrum of undoped and Cl-doped WS_2 nanosheet and (f-i) corresponding colour mapping for W, S, O and Cl atom for doped WS_2

Table 4.4: Atomic Percentage of Undoped and Doped WS_2

WS_2	Atomic %			
	O	S	Cl	W
Undoped	32.17	37.05	0.00	30.78
6 hr dope	51.97	20.15	0.07	27.80
12 hr dope	46.85	24.77	0.14	28.24
18 hr dope	32.78	34.90	0.22	32.19
24 hr dope	26.57	40.72	0.32	32.40

4.5. Electrical Transport Measurement After CI Doping:

The electrical transport properties and semiconducting behaviour of both doped and undoped WS_2 nanosheets were analyzed using Current-Voltage (I-V) measurements. Fig. 4.11(a) provides an illustrative view of the WS_2 device under study, featuring a thin WS_2 nanosheet layer deposited on a clean SiO_2-coated Si substrate, with silver paste serving as the metal contact. The I-V measurements for the fabricated devices were conducted using a Keysight B2900 source meter, with data acquisition performed in ambient conditions over a range of temperatures.

Fig. 4.11(b) presents the I-V characteristics of the fabricated device, revealing distinct non-ohmic behaviour that signifies the presence of R_C and a Schottky barrier at the Metal-WS_2 interface. In forward bias, the current increases with extended doping duration, suggesting that the WS_2 film exhibits n-type semiconducting behaviour. Moreover, as the operating temperature increases, the on-current for both doped and undoped WS_2 thin films also shows a rising trend (see Fig. 4.11(c)), indicating improved conductivity. This trend was observed through temperature-dependent measurements conducted at room temperature (RT), 50 °C, and 100 °C, and is attributed to thermally activated charge carriers, which enhance carrier transport and raise the current level across all devices. At elevated temperatures, thermal energy facilitates electron transitions from the Valence Band (VB) to the Conduction Band (CB), resulting in an increased number of charge carriers and higher carrier density. The Cl doping introduces additional energy states near the CB, further supporting carrier generation at elevated temperatures and leading to higher current levels. These observations highlight that the impact of n-type doping becomes more prominent with longer doping duration.

The contact resistance R_C of the Metal-WS_2 junction was determined using the Transmission Line Model (TLM) for both doped and undoped samples [21]. TLM is a

widely used technique in semiconductor physics to estimate the specific sheet resistance (R_{Sh}) and contact resistivity (ρ_C) at the ohmic or low-resistivity limit. In the TLM method, the total resistance (R_T) is measured for a series of devices with varying channel lengths (L), while maintaining a constant channel width (W). A schematic diagram of the TLM structure is shown in the inset of Fig. 4.11(d). The measured R_T values are then plotted as a function of channel length, and a linear regression is applied to the data. In this plot, the y-axis intercept corresponds to $2R_C$, representing the total contact resistance from both metal-semiconductor interfaces, as demonstrated in Fig. 4.11(d). The total R_T is expressed as the sum of $2R_C$ and the channel resistance, which can be formulated as [67]:

$$R_T = 2R_C + R_{Ch} \tag{4.1}$$

$$R_{Ch} = R_{Sh}\frac{L}{W}$$

Here, R_{Ch} denotes the channel resistance, R_{Sh} represents the sheet resistance of the semiconductor and R_{SD} which is the resistance between two metal contacts, is equal to $2R_C$. A conspicuous change in the R_C is noticed after doping the WS_2 nanosheets with Cl atom. The estimated R_C of the undoped and doped WS_2 is reduced from 0.34 kΩ to 0.15 kΩ. The transfer length (L_T) of the doped WS_2 thin film, obtained using the TLM method, was found to be 18.12 μm extracted and the ρ_C was calculated to be 1.35 x 10^{-6} Ω.cm^2 which was calculated from the following equation [67].

$$\rho_C = R_C L_T W \tag{4.2}$$

$$L_T = \sqrt{\frac{W}{\rho_C}}$$

The L_T represents the characteristic distance over which current flows from the metal contact into the semiconductor material. It defines the region beneath the contact where the voltage drop occurs, with current spreading from the metal into the material. In the R_T vs. channel length plot, the intercept on the x-axis, where R_T= 0, is related to $-2L_T$.

The non-linear I-V characteristics of the fabricated devices indicate the presence of a Schottky barrier at the Metal-WS_2 interface [68]. In the ideal case, when the Φ_M is greater than the Φ_S, a depletion region forms at the M-S interface. The presence of a depletion region at the Metal-WS_2 interface restricts carrier transport across the junction.

This restriction arises from the difference in work functions between the two materials, which creates a potential barrier. The contact potential arises from charge redistribution and the establishment of an electric field across the interface. Consequently, the semiconductor's energy bands bend, forming a potential barrier that impedes electron transition from the semiconductor to the metal. The height of this potential barrier is associated with the difference in work functions between the two materials. The height of this barrier Φ_B in an ideal semiconductor can be theoretically estimated using:

$$\Phi_B = \Phi_M - \chi_S \tag{4.3}$$

Where, χ_s is the electron affinity of the semiconductor. However, in the case of 2D materials like WS_2, the electron affinity is layer-dependent and deviates from bulk semiconductor behaviour due to quantum confinement and surface effects. For WS_2, the electron affinity varies with thickness Monolayer WS_2 typically exhibits an electron affinity in the range of ~4.0-4.5 eV and few-layer to bulk WS_2 shows slightly higher values, approximately ~4.5-4.7 eV, depending on fabrication conditions, environment, and substrate interaction [69]. This layer dependence means that direct estimation of Φ_B from the difference of Φ_M-χ_s becomes unreliable unless the exact layer-dependent electron affinity is known.

In this study, to accurately estimate the SBH at the Metal-WS_2 junction, the thermionic emission theory was applied based on experimental I-V characteristics. The current through a Schottky contact is governed by [68]:

$$I = I_0 \left(\exp \frac{eV}{KT} - 1\right) \tag{4.4}$$

$$\frac{I}{I_0} = \exp \frac{eV}{KT} - 1 \approx \exp \frac{eV}{KT} \qquad [\because eV \gg KT]$$

$$ln(I) = ln(I_0) + \frac{eV}{KT}$$

Where V, I_0, T, e, and K are the applied voltage, saturation current, absolute temperature, charge of an electron and Boltzmann's constant. The saturation current I_0 is obtained by extrapolating the linear part of ln(I) vs. V and taking the intercept of ln(I) in y-axis [17, 58].

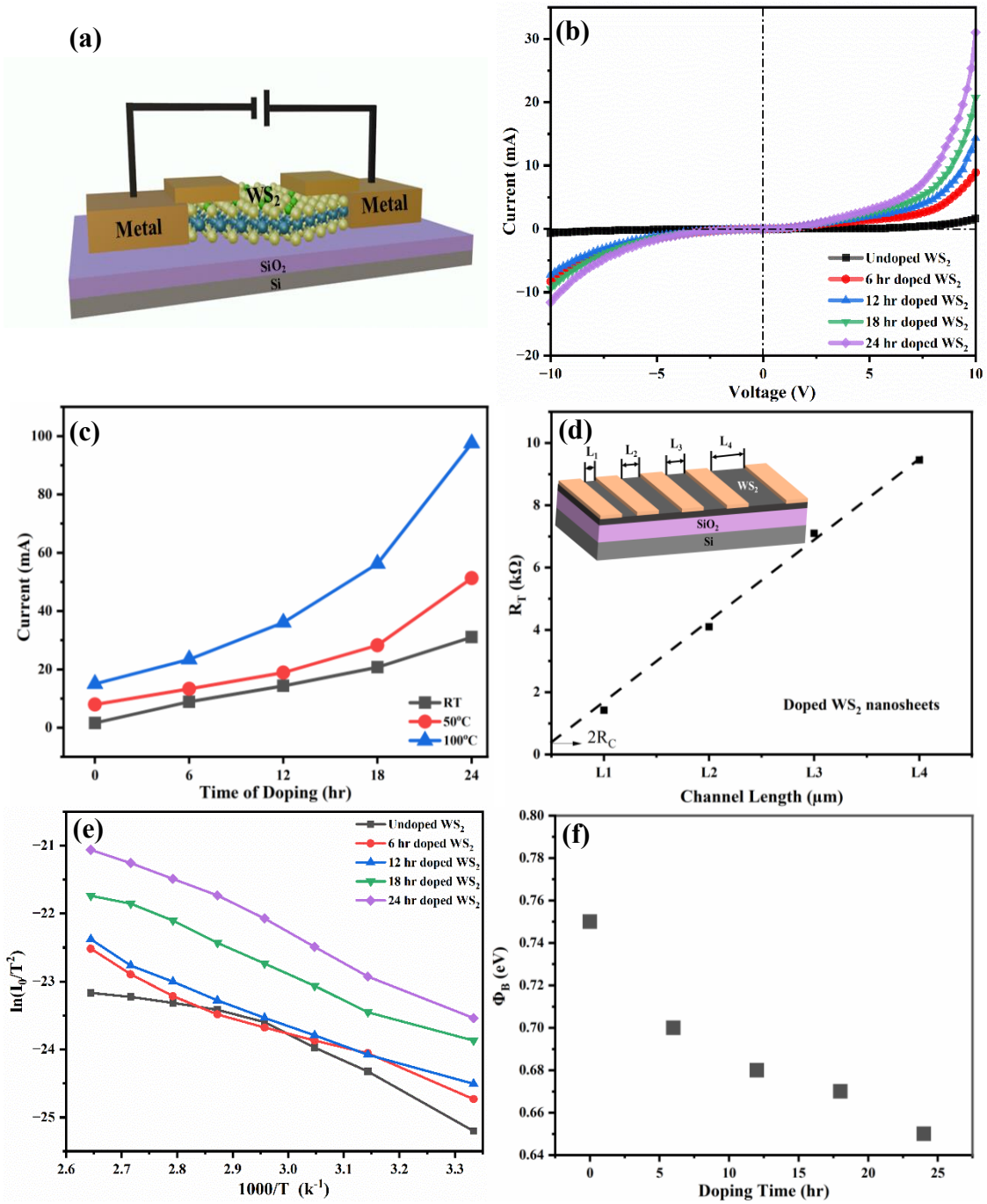

Fig. 4.11: (a) Schematic illustration of two terminal WS_2 devices (b) displays the I-V characteristics and (c) current measured at different temperature ranges plotted as a function of doping duration (d) R_C extraction using TLM method: R_T vs Channel length (e) Activation energy plots for determination of barrier height for undoped and doped WS_2 and (f) displays the variation of Φ_B vs. Doping time

To extract the Φ_B, the I_0 is analyzed as a function of temperature using the thermionic emission theory. The barrier height for the Metal-WS_2 junction can be expressed by the following expression:

$$I_0 = AA^*T^2\, e^{-e\Phi_B/KT} \tag{4.5}$$

$$\Phi_B = \frac{KT}{e}\, ln\left(\frac{AA^*T}{I_0}\right)$$

Where, A is the contact area and A^* represents the effective Richardson constant. The barrier height is extracted from the slope of $\ln(I_0/T^2)$ plotted against 1/T as shown in Fig. 4.11(e). The experimental observations showed that the SBH decreased from approximately 0.75 eV to 0.65 eV for undoped and 24 hr doped WS_2 with the increase of doping time as depicted in Fig. 4.11(f). This reduction is attributed to doping-induced Fermi level shift, which effectively narrows the depletion width and facilitates increased tunneling current across the junction.

Fig. 4.12(a) presents a schematic energy band model for a Metal-WS_2 (M-WS_2) junction. The uppermost part of the diagram represents the vacuum level, which serves as a reference point. The position of the semiconductor's E_F can vary based on the doping level or applied external bias, as shown in Fig. 4.12(b). This illustrates the energy gap between the Metal Fermi level (E_{F_M}) of the metal and the edge of the Conduction Band (E_{CB}) of the semiconductor. The energy band diagram visually represents the energy levels and potential barrier at the Metal-WS_2 junction, which is essential for understanding the behaviour of the junction in relation to carrier transport and other electrical characteristics.

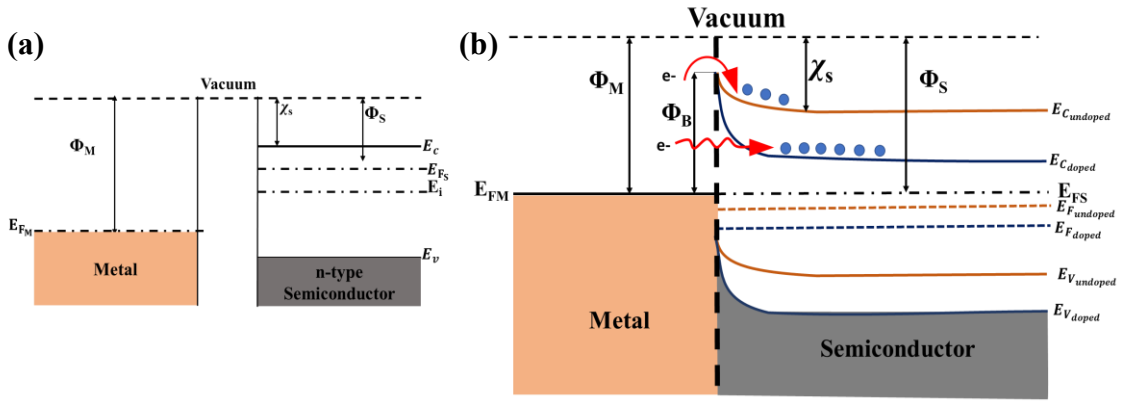

Fig. 4.12: Schematic depiction of energy band diagram for metal and semiconductor junction (a) before their physical contact and (b) M-WS_2 at equilibrium condition for both undoped and doped WS_2

When the semiconductor is doped with n-type dopant atom, the Fermi level of the Semiconductor (E_{F_S}) shifts closer to the E_{CB}, resulting in a very thin barrier at the interface. Due to the difference in work functions, a significant number of electrons from the semiconductor side transfer to the metal side, forming a narrow barrier. In the case of WS_2, doping with Cl atom, it can replace a S vacancy position because S and Cl their atomic radii are similar, both around 100 picometers. Despite the differences in their valency, Cl generally creates Cl^-, whereas S produces S^{2-}; this replacement adds extra electrons to the WS_2 lattice, functioning as n-type dopants. With the increase in Cl concentration, the free electron density in WS_2 increases as well, improving electrical conductivity by introducing additional charge carriers for conduction. Cl doping moves the Fermi level nearer to the conduction band, signifying enhanced n-type characteristics and lowering the Schottky barrier height at M-S junctions. Under forward bias, the energy bands are elevated, allowing for a finite probability of a substantial tunneling current due to the presence of this thin barrier. In this scenario, the total current is contributed by both thermionic emission and tunneling current. The experimental data suggested that the SBH at the Metal-WS_2 junction is reduced, leading to an enhancement in electrical conductivity and facilitating more efficient charge injection. Additionally, increased concentrations of Cl doping can significantly reduce contact resistance at the Metal-WS_2 junction, enhancing overall device performance.

4.6. Summary:

This research demonstrates that molecular doping of WS_2 nanosheets using n-type dopant atoms through surface adsorption technique significantly enhances the electrical charge transport characteristics by increasing charge carriers. A theoretical analysis of doping was conducted using DFT calculations, which investigated the introduction of a Cl atom into the atomic lattice of WS_2. It was observed that a single Cl atom effectively tunes the electronic band structure, causing the CBM to shift closer to the Fermi level. This shift enhances the n-type characteristics of WS_2 compared to its pristine and defective forms. To analyze the material properties, including structural, morphological, and composition, etc. spectroscopic techniques such as Raman spectra, PL, XRD, SEM, and EDX spectroscopy were performed. These studies showed improved stoichiometry, reduced defect states, and identical surface morphology after doping. However, it is

evident from the PL spectra that Cl doping increased the concentration of negatively charged trions, which can be attributed to the higher availability of conduction.

Electrical measurements highlighted the non-ohmic I-V characteristics of undoped WS_2 devices, which were attributed to the presence of Schottky barrier height and contact resistance at the Metal-WS_2 interface. These factors hinder efficient charge transport within the semiconductor. At the interface, the depletion layer is widened, which can restrict the flow of electrons through the junction, leading to a reduction in the device's overall electrical conductivity. Doping not only improves the device's current conductivity but also reduces defects and vacancy states within the nanosheet lattice. Notable changes were observed with prolonged doping durations, which improved conductivity, reflects the reduction of R_C from 0.35 to 0.15 kΩ and SBH from 0.75 eV to 0.65 eV. This reduction facilitates carrier transport through the M-S interface and boosts electrical conductivity in doped WS_2 nanosheets. It is confirmed that the poor electrical conductivity typically observed at the M-WS_2 junction is primarily attributed to atomic vacancies, lattice defects, and low binding energy at the interface and high SBH and R_C. However, doping can facilitate the electron flow through tunneling by lowering the conduction band energy, bringing it closer to the Fermi level and enabling more efficient charge transport. These findings are anticipated to positively impact the understanding and performance optimization of high-performance semiconductor devices based on 2D WS_2 nanosheets.

Bibliography:

[1] Poornimadevi, C., et al. Tuning the electronic properties of WS_2 monolayer by doping transition metals: DFT Approach. Materials Science in Semiconductor Processing, 157: 107339, 2023.

[2] Schulpen, J.J.P.M., et al. Nb Doping and Alloying of 2D WS_2 by Atomic Layer Deposition for 2D Transition Metal Dichalcogenide Transistors and HER Electrocatalysts. ACS Appl. Nano Mater., 7(7): 7395–7407, 2024.

[3] Abbas, O.A., et al. Solution-Based Synthesis of Few-Layer WS_2 Large Area Continuous Films for Electronic Applications. Sci Rep., 10(1): 1696, 2020.

[4] Iqbal, M.W., et al. Tailoring the electrical and photo-electrical properties of a WS_2 field effect transistor by selective n-type chemical doping. RSC Adv., 6(29): 24675–24682, 2016.

[5] Iqbal, M.W., et al. Deep-ultraviolet-light-driven reversible doping of WS_2 field-effect transistors. Nanoscale, 7(2):747–757, 2015.

[6] Rezaei Nik, Y., et al. High-performance CsGeBr3 perovskite/ WS_2 Nano-Flakes Field-Effect Transistor at high temperature. Optical Materials, 132: 112757, 2022.

[7] Lockhart, D. L. R., et al. Relation between film thickness and surface doping of MoS_2 based field effect transistors. APL Materials., 6: 058301, 2018.

[8] Bhattacharjee, S., et al. Intrinsic Limit for Contact Resistance in Exfoliated Multilayered MoS_2 FET. IEEE Electron Device Lett., 37(1):119–122, 2016.

[9] Das, S. & Appenzeller, J. Where Does the Current Flow in Two-Dimensional Layered Systems? Nano Lett., 13(7): 3396–3402, 2013.

[10] Das, S. & Appenzeller, J. Screening and interlayer coupling in multilayer MoS_2. Physica Rapid Research Ltrs., 7(4): 268–273, 2013.

[11] Boehm, A., et al. Engineering of Nanoscale Heterogeneous Transition Metal Dichalcogenide–Au Interfaces. Nano Lett., 23(7): 2792–2799, 2023.

[12] Zhang, Q., et al. Ultrathin All-2D Lateral Diodes Using Top and Bottom Contacted Laterally Spaced Graphene Electrodes to WS_2 Semiconductor Monolayers. ACS Appl. Mater. Interfaces., 15(14):, 18012–18021, 2023.

[13] Hong, J., et al. Exploring atomic defects in molybdenum disulphide monolayers. Nat Commun., 6(1): 6293, 2015.

[14] Tang, H., et al. Effects of Defect and Temperature on the Mechanical Performance of WS_2 : A Multiscale Analysis. J. Phys. Chem. C., 125(4): 2680–2690, 2021.

[15] Wan, Y., et al. Low-defect-density WS_2 by hydroxide vapor phase deposition. Nat Commun., 13(1): 4149, 2022.

[16] Loh, L., et al. Impurity-Induced Emission in Re-Doped WS_2 Monolayers. Nano Lett., 21(12): 5293–5300, 2021.

[17] Kim, Y.J., et al. Contact Resistance Reduction of WS_2 FETs Using High-Pressure Hydrogen Annealing. IEEE J. Electron Devices Soc., 6: 164–168, 2018.

[18] Kim, C., et al. Fermi Level Pinning at Electrical Metal Contacts of Monolayer Molybdenum Dichalcogenides. ACS Nano., 11(2): 1588–1596, 2017.

[19] Liu, X., Choi, M.S., Hwang, E., Yoo, W.J., Sun, J.: Fermi Level Pinning Dependent 2D Semiconductor Devices: Challenges and Prospects. Advanced Materials., 34(15): 2108425, 2022.

[20] Das, S., et al. High Performance Multilayer MoS_2 Transistors with Scandium Contacts. Nano Lett., 13(1):100–105, 2013.

[21] Khalil, H.M.W., et al. Highly Stable and Tunable Chemical Doping of Multilayer WS_2 Field Effect Transistor: Reduction in Contact Resistance. ACS Appl. Mater. Interfaces., 7(42): 23589–23596, 2015.

[22] Zheng, S., et al. Insertion of an ultrathin Al_2O_3 interfacial layer for Schottky barrier height reduction in WS_2 field-effect transistors. Nanoscale., 11(11):, 4811–4821, 2019.

[23] Kaushik, N., et al. Schottky barrier heights for Au and Pd contacts to MoS_2. Applied Physics Letters., 105(11): 113505, 2014.

[24] Murali, K., et al. Accurate Extraction of Schottky Barrier Height and Universality of Fermi Level De-Pinning of van der Waals Contacts. Adv Funct Materials., 31(18): 2010513, 2021.

[25] Nowakowski, K., et al. Control of the metal/WS_2 contact properties using 2-dimensional buffer layers. Nanoscale., 11(12): 5548–5556, 2019.

[26] Vaknin, Y., et al. Schottky Barrier Height and Image Force Lowering in Monolayer MoS_2 Field Effect Transistors. Nanomaterials., 10(12): 2346, 2020.

[27]. Chung, C.-H., et al. WS_2 Transistors with Sulfur Atoms Being Replaced at the Interface: First-Principles Quantum-Transport Study. ACS Omega, 8(11): 10419–10425, 2023.

[28] Tang, H., et al. Schottky Contact in Monolayer WS_2 Field-Effect Transistors. Advcd Theory and Sims., 2(5):1900001, 2019.

[29] Phan, N.A.N., et al. Enhanced Performance of WS_2 Field-Effect Transistor through Mono and Bilayer h-BN Tunneling Contacts. Small, 18(13): 2105753, 2022.

[30] Liu, Y., et al. Approaching the Schottky–Mott limit in van der Waals metal–semiconductor junctions. Nature., 557: 696–700, 2018.

[31] Park, W., et al. Complementary Unipolar WS_2 Field-Effect Transistors Using Fermi-Level Depinning Layers. Adv Elect Materials., 2(2): 1500278, 2016.

[32] Smyth, C.M., et al. Origins of Fermi Level Pinning between Tungsten Dichalcogenides (WS_2 , WTe_2) and Bulk Metal Contacts: Interface Chemistry and Band Alignment. J. Phys. Chem. C., 124: 14550–14563, 2020.

[33] Kwon, G., et al. Interaction- and defect-free van der Waals contacts between metals and two-dimensional semiconductors. Nat Electron., 5: 241–247, 2022.

[34] Lin, L., et al. Shifting Schottky barrier heights with ultra-thin dielectric layers. Microelectronic Engineering, 88(7): 1461–1463, 2011.

[35] Nishimura, T., et al. High-Electron-Mobility Ge n-Channel Metal–Oxide–Semiconductor Field-Effect Transistors with High-Pressure Oxidized Y_2 O_3. Appl. Phys. Express., 4(6): 064201, 2011.

[36] Hu, J., et al. Metal/III-V Schottky barrier height tuning for the design of nonalloyed III-V field-effect transistor source/drain contacts. Journal of Applied Physics., 107(6): 063712, 2010.

[37] Zheng, S., et al. Schottky barrier height reduction for metal/n-InP by inserting ultra-thin atomic layer deposited high- *k* dielectrics. Applied Physics Letters., 103(26): 261602, 2013.

[38] Han, T., et al. Preparation and Research of Monolayer WS_2 FETs Encapsulated by h-BN Material. Micromachines, 12(9): 1006. 2021.

[39] Biscaras, J., et al. Onset of two-dimensional superconductivity in space charge doped few-layer molybdenum disulfide. Nat Commun., 6(1): 8826, 2015.

[40] Kim, Y., et al. Plasma functionalization for cyclic transition between neutral and charged excitons in monolayer MoS_2. Sci Rep., 6(1): 21405, 2016.

[41] Kiriya, D., et al. Air-Stable Surface Charge Transfer Doping of MoS_2 by Benzyl Viologen. J. Am. Chem. Soc., 136(22): 7853–7856, 2014.

[42] Kim, K.H., et al. Effect of large work function modulation of MoS_2 by controllable chlorine doping using a remote plasma. J. Mater. Chem. C., 8(5):1846–1851, 2020.

[43] Sunwoo, H. & Choi, W. Tunable, stable, and reversible n-type doping of MoS_2 via thermal treatment in N-methyl-2-pyrrolidone. Nanotechnology, 33(50): 50LT01, 2022.

[44] Chanana, A. & Mahapatra, S. Density functional theory based study of chlorine doped WS_2-metal interface. Applied Physics Letters., 108(10):103107, 2016.

[45] Chang, R.-J., et al. Postgrowth Substitutional Tin Doping of 2D WS_2 Crystals Using Chemical Vapor Deposition. ACS Appl. Mater. Interfaces., 11(27): 24279–24288, 2019.

[46] Wang, H., et al. An ambipolar transistor based on a monolayer WS_2 using lithium ions injection. Mater. Res. Express., 7(7): 076302, 2020.

[47] Chee, S.-S., et al. Sulfur vacancy-induced reversible doping of transition metal disulfides via hydrazine treatment. Nanoscale., 9(27): 9333–9339, 2017.

[48] Liu, M., et al. Enhanced carrier transport by transition metal doping in WS_2 field effect transistors. Nanoscale., 12(33): 17253–17264, 2020.

[49] Yang, L., et al. Chloride Molecular Doping Technique on 2D Materials: WS_2 and MoS_2. Nano Lett., 14(11):6275–6280, 2014.

[50] Zhang, S., et al. Control of the Schottky barrier height in monolayer WS_2 FETs using molecular doping. AIP Advances., 12(8): 085222, 2022.

[51] Jang, J., et al. Reduced dopant-induced scattering in remote charge-transfer-doped MoS_2 field-effect transistors. Sci. Adv., 8(38): eabn3181, 2022.

[52] Kang, K., et al. The effects of substitutional Fe-doping on magnetism in MoS_2 and WS_2 monolayers. Nanotechnology., 32(9): 095708 (2021.

[53] Pollmann, E., et al. Large-Area, Two-Dimensional MoS_2 Exfoliated on Gold: Direct Experimental Access to the Metal–Semiconductor Interface. ACS Omega, 6(24): 15929–15939, 2021.

[54] Yang, K., et al. Tuning electronic behaviors of WS_2 by molecular doping. Materials Today Communications, 33: 104226, 2022.

[55] Wang, W., et al. The Electronic Properties of O-Doped Pure and Sulfur Vacancy-Defect Monolayer WS_2: A First-Principles Study. Materials., 11(2): 218, 2018.

[56] Rastogi, P., et al. Doping Strategies for Monolayer MoS_2 via Surface Adsorption: A Systematic Study. J. Phys. Chem. C., 118(51): 30309–30314, 2014.

[57] Dhakal, K.P., et al. Confocal absorption spectral imaging of MoS_2: optical transitions depending on the atomic thickness of intrinsic and chemically doped MoS_2. Nanoscale, 6(21): 13028–13035, 2014.

[58] Kim, H.-C., et al. Engineering Optical and Electronic Properties of WS_2 by Varying the Number of Layers. ACS Nano, 9(7): 6854–6860, 2015.

[59] Sumathi, P., et al. Influence of Cu Irons on Structural, Optical, and Electrical Properties of Pure WS_2 Thin Films and Development of p-Si/n-Cu@WS_2 Photodiode for Optoelectronic Application. J Inorg Organomet Polym.. 32(1): 63–74, 2022.

[60] Splendiani, A., et al. Emerging Photoluminescence in Monolayer MoS_2. Nano Lett. 10(4): 1271–1275, 2010.

[61] Qin, Z., et al. Effect of layer number on recovery rate of WS_2 nanosheets for ammonia detection at room temperature. Applied Surface Science., 414: 244–250, 2017.

[62] Pan, Y., et al. Enhanced electrochemical hydrogen evolution performance of WS_2 nanosheets by Te doping. Journal of Catalysis., 382: 204–211, 2020.

[63] Sumathi, P., et al. Synthesis and characterization of tungsten disulfide thin films by spray pyrolysis technique for n-WS_2/p-Si junction diode application. J Mater Sci: Mater Electron., 29 (19): 16815–16823, 2018.

[64] Pradhan, G. & Sharma, A.K. Linear and nonlinear optical response of sulfur-deficient nanocrystallite WS_2 thin films. J Mater Sci., 54(24): 14809–14824, 2019.

[65] Roy, A., et al. Structural, spectroscopic and electrical properties of liquid phase exfoliated few layered two-dimensional tungsten disulfide (WS_2) using anionic surfactant. J Mater Sci: Mater Electron., 34(3): 224, 2023.

[66] Hazarika, S.J. & Mohanta, D. Inorganic fullerene-type WS_2 nanoparticles: processing, characterization and its photocatalytic performance on malachite green. Appl. Phys. A., 123(5) 381, 2017.

[67] Giza, M., et al. Contact Resistance Engineering in WS_2 -Based FET with MoS_2 Under-Contact Interlayer: A Statistical Approach. ACS Appl. Mater. Interfaces., 16(36): 48556–48564, 2024.

[68] Kim, J., et al. Schottky Diode with Asymmetric Metal Contacts on WS_2. Adv Elect Materials., 8(3): 2100941, 2022.

[69] Roy, S. & Bermel, P. Electronic and optical properties of ultra-thin 2D tungsten disulfide for photovoltaic applications. Solar Energy Materials and Solar Cells., 174:370–379, 2018.